MNRAS 000, 1–9 (2017) Preprint March 21, 2017 Compiled using MNRAS LATEX style file v3.0

Predicting Pulsar Scintillation from Refractive Current Sheets

Dana Simard,[1,2,3]★ Ue-Li Pen[1,3,4,5]†
[1] Canadian Institute for Theoretical Astrophysics, University of Toronto, 60 Saint George Street, Toronto, ON M5S 3H8, Canada
[2] Department of Astronomy and Astrophysics, University of Toronto, 50 Saint George Street, Toronto, ON M5S 3H4, Canada
[3] Dunlap Institute for Astronomy and Astrophysics, University of Toronto, 50 Saint George Street, Toronto, ON M5S 3H4, Canada
[4] Canadian Institute for Advanced Research, Program in Cosmology and Gravitation, Toronto, ON M5G 1Z8, Canada
[5] Perimeter Institute for Theoretical Physics, 31 Caroline Street North, Waterloo, ON N2L 2Y5, Canada

arXiv:1703.06855v1 [astro-ph.GA] 20 Mar 2017

Accepted XXX. Received YYY; in original form ZZZ

ABSTRACT

Recent observations of scintillating pulsars' dynamic and secondary spectra show evidence for collinear compact ionized structures in the interstellar medium. One proposed explanation for these structures is that they are the crests of Alfvén waves propagating along current sheets closely aligned to our line-of-sight to the pulsar. Using geometric optics, we develop a simple model of these folded current sheets that makes observable predictions for how the secondary spectrum of the pulsar will vary over time and frequency. We find that caustics occur only if the current sheet is overdense compared to the interstellar medium, and that the lensed image of the pulsar appears closer to the line-of-sight image at higher frequencies if the current sheet is underdense, but at lower frequencies if the current sheet is overdense.

Key words: pulsars: general – ISM: general – ISM: structure – magnetic fields – plasmas – scattering

1 INTRODUCTION

Recent observations of pulsar scintillation, the change in the observed flux of a pulsar with frequency and time, have shown significant structure in the secondary spectrum (the 2-dimensional power spectrum of the dynamic spectrum, flux over time and frequency). In particular, parabolic arcs have been found to be ubiquitous in the secondary spectra of pulsars imaged with sufficient dynamic range and resolution (Stinebring et al. 2001; Putney et al. 2005), indicating highly anisotropic scattering that is localized along the line-of-sight to the pulsar. In some pulsars, inverted arclets with apexes along the main arc are also present (Hill et al. 2005; Stinebring 2007); see Brisken et al. (2010, figure 1) for a particularly nice example. This structure requires discrete images along a scattering sheet localized partway along the line-of-sight to the pulsar (Walker et al. 2004; Cordes et al. 2006); each inverted arclet is created by the interference of one lensed image with all of the other images of the pulsar. These discrete images have been observed to persist for weeks (Hill et al. 2003, 2005), suggesting long-lived density substructure within the scattering sheet. The anisotropic scattering and long-lived substructure are inconsistent with the expected characteristics of turbulence in the interstellar medium (ISM), long believed to be the cause of pulsar scintillation. In addition, such large free electron densities are required to produce the observed scattering angles that these structures would be out of pressure equilibrium with the ISM and therefore rare, in contrast to the prevalence of pulsar scintillation.

Pen & Levin (2014) suggest that scintillation is instead caused by current sheets along magnetic domain boundaries. Alfvén waves along these sheets with long wavelengths and sufficient amplitudes can fold these sheets, creating a series of crests. If the current sheet is closely aligned with our line-of-sight to the pulsar and folded in a perpendicular direction, a high gradient in free electron column density is achieved at the crest of the fold, and lensing occurs. Grazing refraction off of many of these crests results in a linear series of images, in analogy to grazing reflection off waves on a lake. In this model, the curvature of the current sheet relieves the requirement for very high electron densities; it is the combination of the curvature and the difference in the electron density between the current sheet and the rest of the ISM that leads to large refraction angles. This not only solves the issue of these structures having short lifetimes due to large overpressures, but also has the implication that both underdense and overdense lenses can produce the large bending angles observed; we will thus consider both cases here.

★ E-mail: simard@astro.utoronto.ca
† E-mail: pen@cita.utoronto.ca

© 2017 The Authors

Quantitative models are useful for exploring the effects of proposed lensing structures and their consistency with observations. A number of models have been considered in the context of both pulsar scintillation and quasar extreme scattering events (ESEs) (Fiedler et al. 1987), lensing of quasars by the ISM, a phenomenon that exhibits both qualitative similarities (flux variations with time) and differences (symmetric light curve, very large flux variations) to pulsar scintillation. Clegg et al. (1998) model two ESEs using a Gaussian-shaped lens with a free electron overdensity. They find that the lens can produce the overall shape of the light curves observed, but that the parameters of the lens must be fine-tuned at each frequency. Pen & King (2012) consider the effects of a Gaussian-shaped underdense lens on a point source such as a pulsar or quasar, and find that a double-peaked light curve, such as those characteristic of ESE's, is produced. Other authors (Tuntsov et al. 2015; Bannister et al. 2016) model the dynamic spectrum of an ESE in an attempt to determine the electron column density and shape of the lens. They consider two lens shapes, one which is isotropic and one which is anisotropic, but find that the data holds no preference for one over the other. Once again, they find that the parameters used to model the ESE at one frequency are not suitable at other frequencies. These results indicate that reproducing the lensing behaviour at a single frequency band and epoch is not enough to suggest consistency of the model with observations; changes over time and frequency must also be consistent.

In this paper, we investigate the effects of a thin folded plasma sheet, like the current sheets folded by Alfvén waves discussed by Pen & Levin (2014), on emission from a pulsar. In Section 2 we construct a quantitative model of this mechanism. Then, in Section 3 we present the results of this model. We examine the conditions required to produce multiple images at a single fold, and determine the magnifications and angular separations between the two images. We also explore how these magnifications and angular separations change with time and frequency. Finally, the implications of this work and anticipated extensions are discussed in Section 4.

2 LENSING MODEL

We begin our investigation by considering a single wave crest. We choose z to be the line-of-sight direction, and x and y to be in the plane of the sky, with the origin at the crest of the fold. We will consider a sheet of thickness T extending in the z and y directions, and folded in the x direction, so that all refraction occurs in the x direction. We will model the crest itself as a parabola in the x-z plane. In truth, we do not know the orientation of the sheet or the fold in the x-z plane, but since it is the projected curvature of the fold that causes lensing, differences in inclination can be accounted for by changing the curvature of the parabola. We write the equation for the fold as

$$x = \frac{z^2}{2R}\,, \tag{1}$$

where R is the radius of curvature projected along the x direction at the apex of the parabola. In physical parameters, for a sheet with an inclination angle i relative to the line-of-sight to the pulsar, the radius of curvature is

$$R = \frac{\lambda_A^2 \cos(i)}{4\pi^2 A}\,, \tag{2}$$

where λ_A and A are respectively the wavelength and amplitude of the Alfvén wave creating the fold.

We will use the lensing geometry shown in Fig. 1. In this geometry, the lens equation is

$$\theta = \beta + s\hat{\alpha}\,, \tag{3}$$

where θ is the observed position of the source, β is the true position, $\hat{\alpha}$ is the bending angle, $s = 1 - d_{\rm lens}/d_{\rm psr}$, $d_{\rm psr}$ is the distance to the pulsar plane, and $d_{\rm lens}$ is the distance to the lens plane. We determine $\hat{\alpha}$ by considering Φ, the phase change imparted by the lens,

$$\Phi(x) = \frac{2\pi}{\lambda}\int dz(n(x) - n_0)\,, \tag{4}$$

where n_0 is the index of refraction outside of the lens, n is the index of refraction inside the lens, and λ is the wavelength of observations. The bending angle is related to the gradient of the phase change by

$$\hat{\alpha}(x) = -\frac{\lambda}{2\pi}\nabla_x\Phi(x)\,. \tag{5}$$

Assuming that the index of refraction is constant inside of the lens, this reduces to

$$\hat{\alpha}(x) = -\Delta n\nabla_x Z(x)\,, \tag{6}$$

where $\Delta n = n - n_0$ and Z is the extent of the lens along the line-of-sight. In the regime $x > T/2$, $Z = 2T\frac{dl}{dx}$, where dl is the length element of the lens, $dl^2 = dz^2 + dx^2$. The factor of 2 comes from the two sides of the parabola. Using equation (1) for the shape of the lens, we find

$$\nabla_x Z = 2T\frac{d^2 l}{dx^2} = -\frac{2TR}{x^2\sqrt{R/2x+1}}\,, \tag{7}$$

so that we can write

$$\hat{\alpha}(x) = \Delta n\frac{2TR}{x^2\sqrt{R/2x+1}}\,. \tag{8}$$

For a plasma, the index of refraction is given by

$$n = \sqrt{1 - \frac{\omega_p^2}{\omega^2}}\,, \tag{9}$$

where $\omega_p = \sqrt{4\pi c^2 r_e n_e}$ is the characteristic frequency of the plasma expressed in terms of the electron density, n_e, and the classical electron radius, $r_e = \frac{1}{4\pi\epsilon_0}\frac{e^2}{m_e c^2}$ where ϵ_0 is the vacuum permittivity and m_e is the mass of the electron. For $n_e = 0.03$ cm^{-3}, a typical value for the ISM, this characteristic frequency is 1.5 kHz, much smaller than the GHz frequencies of typical radio observations. Therefore, we simplify the index of refraction to

$$n = 1 - \frac{\lambda^2}{2\pi}n_e r_e\,. \tag{10}$$

We now write the bending angle in terms of the electron density,

$$\hat{\alpha}(x) = -\frac{\lambda^2}{2\pi}\Delta n_e r_e\frac{2TR}{x^2\sqrt{R/2x+1}}\,, \tag{11}$$

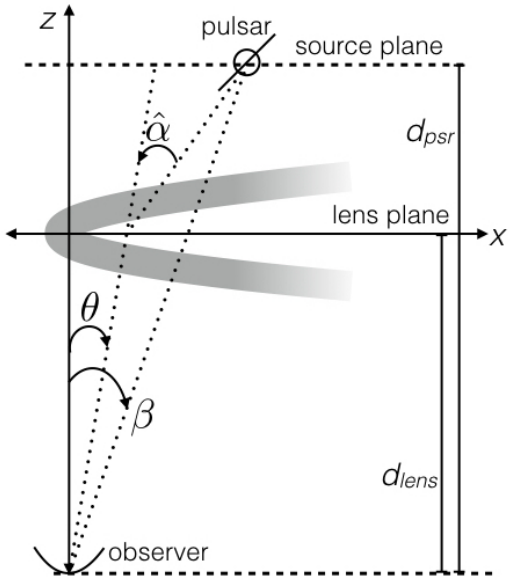

Figure 1. Lensing geometry and definitions of variables that we will use in this paper. The grey curve shows the location of the fold. The angles θ and β are measured clockwise from the line from the observer to the crest of the fold. The angle $\hat{\alpha}$ is measured clockwise from the line between the pulsar and the image of the pulsar on the lens plane. Note that this geometry is not to scale; in practice the angles are all much smaller than 1 and the fold covers only a very small portion of the line-of-sight to the pulsar.

where Δn_e is the difference between the free electron densities inside and outside of the current sheet. Since we measure angular positions on the sky, rather than physical ones, we will use the dimensionless variables $\theta = x/d_{\rm lens}$, $\theta_R = R/d_{\rm lens}$ and $\theta_T = T/d_{\rm lens}$, and write:

$$\hat{\alpha}(\theta) = -\frac{\lambda^2}{2\pi}\Delta n_e r_e \frac{2\theta_T\theta_R}{\theta^2}\frac{1}{\sqrt{\theta_R/2\theta+1}} \,. \tag{12}$$

We now write the lens equation for this system,

$$\theta = \beta - s\frac{\lambda^2}{2\pi}\Delta n_e r_e \frac{2\theta_T\theta_R}{\theta^2}\frac{1}{\sqrt{\theta_R/2\theta+1}} \,. \tag{13}$$

We see that increasing the over or underdensity, radius of curvature, or thickness of the lens results in a larger deflection. We can also calculate the convergence for this system,

$$\kappa = \frac{1}{2}\nabla_\theta\alpha = \frac{s\lambda^2}{2\pi}\Delta n_e r_e \frac{\theta_T\theta_R}{\theta^3}\frac{2+3\theta_R/4\theta}{(\theta_R/2\theta+1)^{3/2}} \,. \tag{14}$$

When $\Delta n_e < 0$, the current sheet is underdense, $\kappa < 0$ and the lens is convergent. When $\Delta n_e > 0$, the current sheet is overdense, $\kappa > 0$ and the lens is divergent.

Under the approximation that $\theta \ll \theta_R/2$, equation (13) simplifies to

$$\theta = \beta - s\frac{\sqrt{2}r_e\lambda^2}{\pi}\frac{\Delta n_e\theta_T\sqrt{\theta_R}}{\theta^{3/2}} \tag{15}$$

$$= \beta + 2\sqrt{2}s\frac{\Delta n\,\theta_T\sqrt{\theta_R}}{\theta^{3/2}} \,, \tag{16}$$

where we have used equation (10) to write the lens equation in terms of Δn. We see that the lens equation depends only on the frequency of observation, the distances to the pulsar and lens, and a single physical parameter describing the lens itself, $\Delta n_e\theta_T\sqrt{\theta_R}$; in other words, the column density and radius of curvature of the lens are degenerate. Throughout this paper, we will use this approximation to analyze the behaviour of the lens; however all numerical results are calculated using the full form of the lens equation, equation (13).

2.1 Lens Parameters

For our numerical model, we will assume the distances to the pulsar and lens are those measured by Liu et al. (2016) for PSR B0834+06 and one of its lensing screens, $d_{\rm psr} = 620$ pc and $d_{\rm lens} = 389$ pc, as this is one of the most thoroughly studied examples of pulsar scintillation. We will assume an observing frequency of 314.5 MHz.

Although the electron density difference across the lens Δn_e, the dimensionless lens thickness θ_T, and dimensionless lens curvature θ_R are degenerate in the lens equation, these parameters are not completely independent or unconstrained. In order to fold the current sheet, the amplitude of the Alfvén wave must be much greater than the thickness of the sheet, and we expect a very small inclination angle of the sheet with respect to our line-of-sight, $i \ll 1$, in order to create the linear series of images observed. We expect the projected wavelength, $\lambda_A \sin(i)$, to be similar to the separation between images, which varies between about 0.1 to 1 AU for the PSR B0834+06 system (Brisken et al. 2010). The projected amplitude of the fold sets a minimum angular separation between the two images. For $\theta > A\cos(i)/d_{\rm lens}$, no fold exists and therefore we expect no lensed image to be formed. This leads to a gap at low delays in the secondary spectrum, but due to the large flux at zero delay in the secondary spectrum a small gap at low delays would be difficult to observe. The amplitude chosen must be large enough to lead to a small minimum angular separation reconcilable

with observations. Finally, constraints on the thickness can be placed directly using our model, as we will discuss in Section 3.2 below.

For our numerical results, we will assume some parameters of the lens informed by these constraints, and model only the electron density inside the lens. However, keep in mind that, apart from the discussion in Section 3.2, our model can only be used to constrain the combination of parameters $\Delta n_e \theta_T \sqrt{\theta_R}$ and not Δn_e itself. We choose an Alfvén wavelength $\lambda_A = 10^5$ AU, an inclination of the sheet with respect to our line-of-sight to the pulsar $i = 10^{-5}$ rad, a thickness of the sheet $T = 0.03$ AU or $\theta_T = 0.078$ mas, and an amplitude of the Alfvén wave $A = 0.3$ AU. These parameters give a projected wavelength of 1 AU, and a projected radius of curvature at the apex of the parabola of $R = 4.1$ kpc or $\theta_R = 2.2\text{x}10^6$ arcsec. While we will see later that θ_T is both physically and observationally interesting, θ_R does not match to a physical angle within the system, and only represents the degree to which the fold is curved. We will assume a typical electron density in the ISM of $n_e = 0.03$ cm^{-3}, and we will consider electron density differences between inside and outside the lens of $\Delta n_e = \pm 0.3, \pm 0.003$ cm^{-3}. While $\Delta n_e = -0.3$ cm^{-3} results in a negative electron density inside the lens, the degeneracy between lens parameters means that we can construct a lens with similar behaviour but positive electron density. For the chosen parameters, the approximation above, that $\theta \ll \theta_R/2$, holds true for $\theta \ll 10^6$ arcsec.

3 RESULTS

We can solve equation (13) in order to calculate the number, locations, and magnifications of the lensed images as the pulsar moves behind the lens. We will go through this process for a single fold in order to determine when multiple images are formed and how the magnifications and separations of those images change over time and frequency.

The solution to the lens equation, equation (13), gives the observed angular positions, θ, of the pulsar for a given true angular position, β. Due to conservation of surface brightness, the magnification of the lensed image is

$$\mu = \left(\frac{d\beta}{d\theta} \right)^{-1} . \tag{17}$$

Using equation (15), this evaluates to

$$\mu \simeq \left(1 + 3\sqrt{2} s \frac{\Delta n \theta_T \sqrt{\theta_R}}{\theta^{5/2}} \right)^{-1} . \tag{18}$$

The angular position and magnification are shown in Fig. 2. When examining these two figures, recall that the lens itself is at $\theta \geq 0$, with maximum curvature at $\theta = 0$. From Fig. 2, we see that multiple images are produced by the underdense, convergent lens when the pulsar is not behind the fold, and multiple images are produced by the overdense, divergent lens when the pulsar is behind the fold. We also note that strong caustics, where the observed flux is many orders of magnitude larger than the intrinsic flux of the pulsar, occur only in the overdense case. For this case, the fainter image is also inverted, as indicated by the negative magnification, and there is a range in β for which we see no images at all. At small, positive β, the line-of-sight to the pulsar is obscured by the lens, so that no line-of-sight image is visible, and the divergent lens is bending light out of our sight. In the regime where two images are produced, the fainter of the two images becomes fainter as the angular separation between the two images increases, as shown in Fig. 3.

Before we construct observables from our model, we will review the information obtainable from observations. From the power distribution in the secondary spectrum, the magnification of a lensed image can be determined relative to the line-of-sight image of the pulsar. From the secondary cross-spectrum, the 2-D Fourier transform of the on-pulse visibility between two telescopes in Very Long Baseline Interferometry (VLBI), the angular separations between images can be measured. If the distance to the pulsar is known, the secondary spectrum can then be used to measure the distance to the lens and the pulsar-lens relative velocity. See Brisken et al. (2010) for more detail on extracting this information from VLBI observations and an example. To compare with observations, we will therefore investigate the magnification ratios and angular separations between images in the cases where two images occur at a single fold.

Analytically, we can understand the relation between the magnification ratio and angular separation for $|\beta| \gg \left(s \Delta n \, \theta_T \sqrt{\theta_R}\right)^{2/5}$, $|\beta| \gg 2$ mas for the parameters chosen in Section 2.1, where the location and magnification of the brightest image are $\theta_0 \simeq \beta$ and $\mu_0 \simeq 1$ respectively. In this case, the angular separation is

$$\Delta\theta \simeq \theta - \beta \simeq -2\sqrt{2} s \frac{\Delta n \theta_T \sqrt{\theta_R}}{\theta^{3/2}} \tag{19}$$

$$\simeq -13. \frac{s}{1/2} \frac{\Delta n}{1.3\text{x}10^{-11}} \frac{\theta_T}{4\text{x}10^{-10}} \sqrt{\frac{\theta_R}{10}} \left(\frac{\theta}{1\text{mas}} \right)^{-3/2} \text{mas} , \tag{20}$$

where θ is the angular location of the fainter image. This allows us to write θ in terms of the angular separation, $\Delta\theta$:

$$\theta \simeq \left(-2\sqrt{2} s \frac{\Delta n \theta_T \sqrt{\theta_R}}{\Delta\theta} \right)^{2/3} . \tag{21}$$

We see from Fig. 2 that in this regime the magnifications of the faint images are much less than one. We can therefore simplify equation (18):

$$\mu \simeq \frac{1}{3\sqrt{2}} \frac{1}{s} \frac{\theta^{5/2}}{\Delta n \, \theta_T \sqrt{\theta_R}} . \tag{22}$$

We now combine equations (21) and (22) to write the magnification ratio in terms of the angular separation:

$$\left| \frac{\mu}{\mu_0} \right| \simeq \frac{2}{3} \left(2\sqrt{2} s \, \Delta n \, \theta_T \sqrt{\theta_R} \right)^{2/3} |\Delta\theta|^{-5/3} \tag{23}$$

$$\simeq 0.08 \left(\frac{s}{1/2} \frac{\Delta n}{1.3\text{x}10^{-11}} \frac{\theta_T}{4\text{x}10^{-10}} \sqrt{\frac{\theta_R}{10}} \right)^{2/3} \left| \frac{\Delta\theta}{10\text{mas}} \right|^{-5/3} . \tag{24}$$

Equation (23) can be rewritten as

$$\left| \frac{\mu}{\mu_0} \right| \simeq \frac{2}{3} \left| \frac{\Delta\theta_{\text{ref}}}{\Delta\theta} \right|^{5/3} , \tag{25}$$

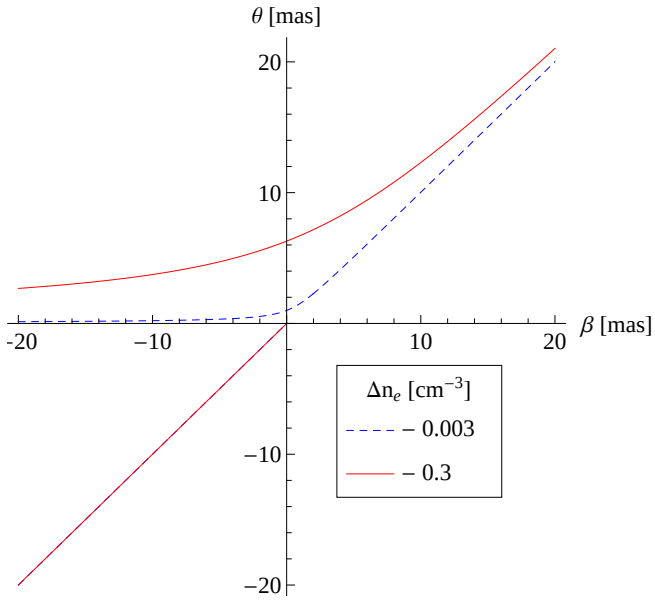

(a) Underdense, convergent lens

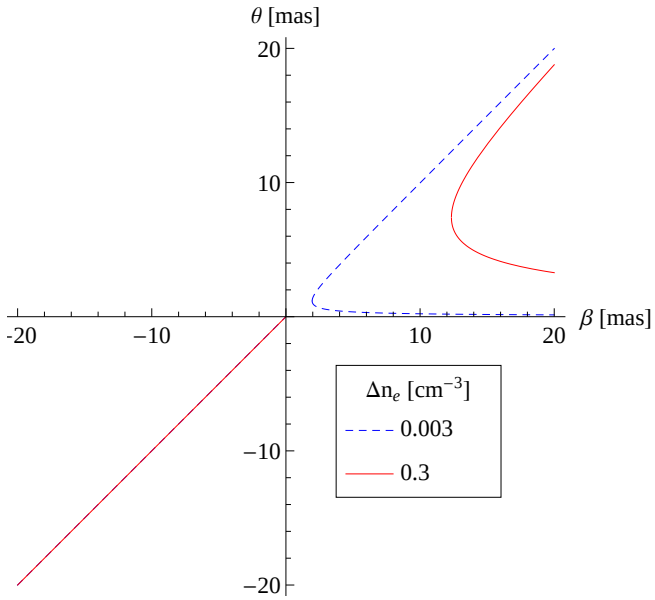

(b) Overdense, divergent lens

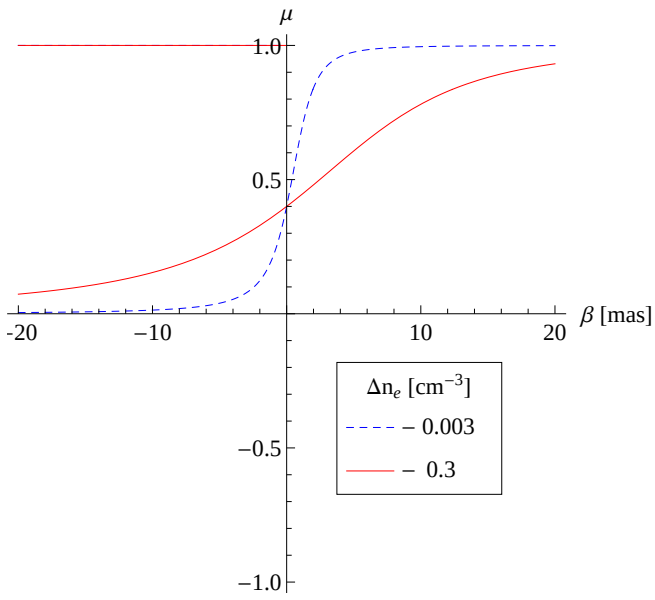

(c) Underdense, convergent lens

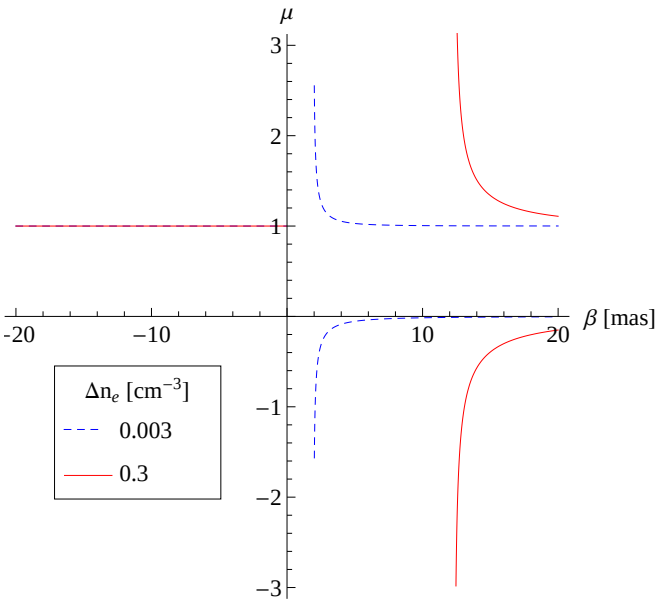

(d) Overdense, divergent lens

Figure 2. The observed position of the pulsar, θ, and magnification, μ, as a function of the true position, β. Recall that the fold is at $\theta \geq -\theta_T/2$, with the crest of the fold at $\theta = 0$. In the underdense lens case, a lensed image is observed along with the true, unlensed image of the pulsar before the pulsar passes behind the fold ($\beta \leq -\theta_T/2$), as the convergent lens is bending light from the pulsar into our line-of-sight. The angular separation between these two images reaches a minimum, non-zero value just as the pulsar passes behind the crest of the fold ($\beta = 0$), and the magnification of the lensed image at this point is independent of Δn_e. After the pulsar passes behind the fold, the line-of-sight image to the pulsar is obscured by the lens, and a single, lensed image is observed. In the case of an overdense lens, only the line-of-sight image is seen until the pulsar is passing behind the fold as the divergent lens is bending light out of our line-of-sight. Just after the pulsar has passed behind the lens, no images are seen, as the line-of-sight image is obscured by the lens, and the divergent lens is still bending light out of our line-of-sight. There is a minimum β for which two images are produced, and at which the two images have zero angular separation and are both caustics; the angular separation between the images grows as the pulsar moves to larger β. The legend indicates the difference between the free electron density inside and outside of the lens, Δn_e when the radius of curvature and thickness of the lens are assumed to be 4.1 kpc and 0.03 AU respectively. In the region $\theta < -\theta_T/2$, the solid line lies directly on top of the dashed line.

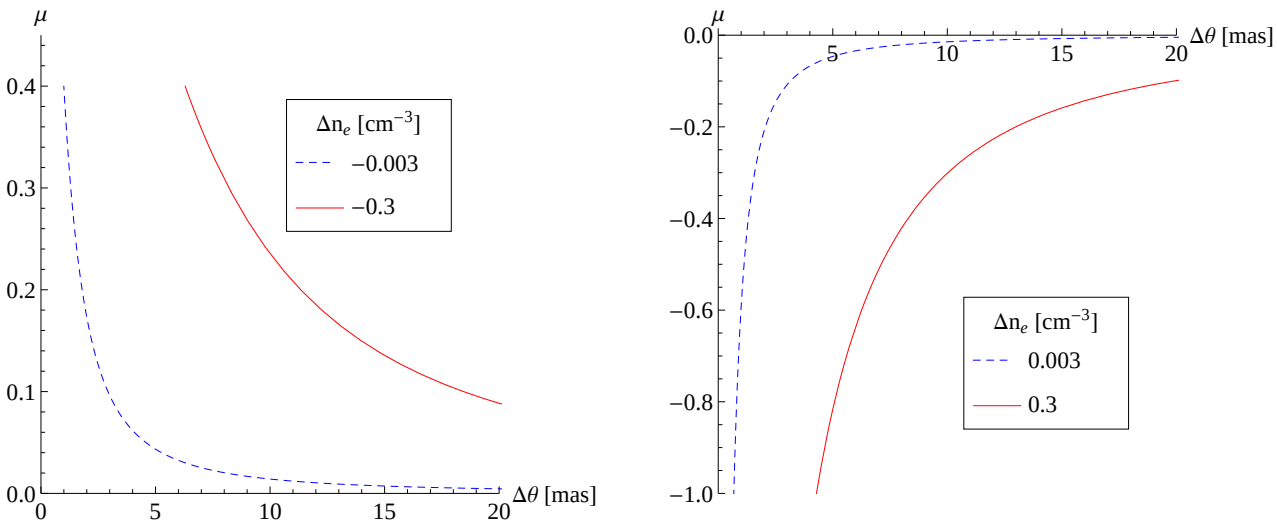

(a) Underdense, convergent lens

(b) Overdense, divergent lens

Figure 3. The magnification of the fainter image, μ, as a function of the angular separation between the two images formed at a single fold, $\Delta\theta$ for both the convergent and divergent lenses. Recall from Fig. 2 that two images are formed by the convergent lens when $\beta < -\theta_T/2$ and by the divergent lens when $\beta > 0$.

where

$$\Delta\theta_{\rm ref} = \left(2\sqrt{2}s\,\Delta n\,\theta_T\sqrt{\theta_R}\right)^{2/5} \tag{26}$$

$$\simeq 2.8\,{\rm mas}\left(\frac{\Delta n}{1.3{\rm x}10^{-11}}\frac{\theta_T}{4{\rm x}10^{-10}}\sqrt{\frac{\theta_R}{10}}\right)^{2/5}. \tag{27}$$

Therefore, we expect $\left|\frac{\mu}{\mu_0}\right| \propto |\Delta\theta|^{-5/3}$ for large separations. Recall that in the convergent case $\frac{\mu}{\mu_0} > 0$, while in the divergent case, the faint image is inverted, so that $\frac{\mu}{\mu_0} < 0$.

The numerical relation between the angular separation and flux ratio of two images formed at a single fold is shown in Fig. 4. We see that after each curve is shifted by the reference separation, $\Delta\theta_{\rm ref}$, the relation between magnification ratio and angular separation is independent of the lens parameters. By measuring the angular separation and flux ratio for a pair of images, we can determine the value of $\Delta\theta_{\rm ref}$ required to place the point along the curves in Fig. 4, and therefore $\Delta n_e\,\theta_R\sqrt{\theta_T}$, provided that the distance to the pulsar is known. If the pulsar distance is not known, we can still determine the effective distance, $D_{\rm eff} = s/d_{\rm lens}$, from the secondary cross-spectrum and calculate $\Delta n_e\,\theta_R\sqrt{\theta_T d_{\rm lens}}$ from the reference angular separation. Since we do not know if the lens is overdense or underdense, we must consider both cases at this stage; in Section 3.1 we will see that changes in the scintillation pattern with frequency do depend on the sign of Δn_e and therefore can be used to differentiate between overdense and underdense sheets.

3.1 Time and frequency evolution of the system

As we have just seen, by measuring the magnification ratio and angular separation between a pair of images, we can constrain the free parameter of the lens, $\Delta n_e\,\theta_T\sqrt{\theta_R}$, provided that the ratio of the distances to the lens and pulsar is known; otherwise, we can constrain $\Delta n_e\,\theta_T\sqrt{\theta_R d_{\rm lens}}$. Once either of these parameters is constrained, changes in the locations and magnifications of the images with frequency can be predicted. If the angular velocity of the pulsar relative to the screen in the x-direction (parallel to the axis along which the images are formed; see Fig. 1), $\frac{(V_{\rm psr}-V_{\rm lens})_\parallel}{d_{\rm psr}}$, is also known, we can predict changes over time. If we assume that the pulsar velocity dominates the relative velocity, then $\frac{(V_{\rm psr}-V_{\rm lens})_\parallel}{d_{\rm psr}} \approx \mu_{p,\parallel}$, where μ_p is the proper motion of the pulsar. The screen velocity parallel to the x-axis can be calculated from the secondary spectrum of the system if the proper motion of the pulsar and the geometry of the scattering are known, as done by Liu et al. (2016), to obtain a more accurate relative angular velocity.

As an example, consider two images with a magnification ratio of 0.01 and an angular separation of 10 mas at a frequency of 314.5 MHz. Using these values, we calculate that the lens has, for the parameters given in Section 2.1, $|\Delta n_e| = 0.0018$ cm^{-3}. From the lens equation and the angular separation, we now determine the true position of the pulsar relative to the crest of the fold, β, for the underdense and overdense cases, -9.79 and 10.21 mas respectively. We will assume a velocity of the pulsar relative to the scattering screen and parallel to the line of images of 172.4 km s^{-1}, the relative velocity between PSR B0834+06 and one

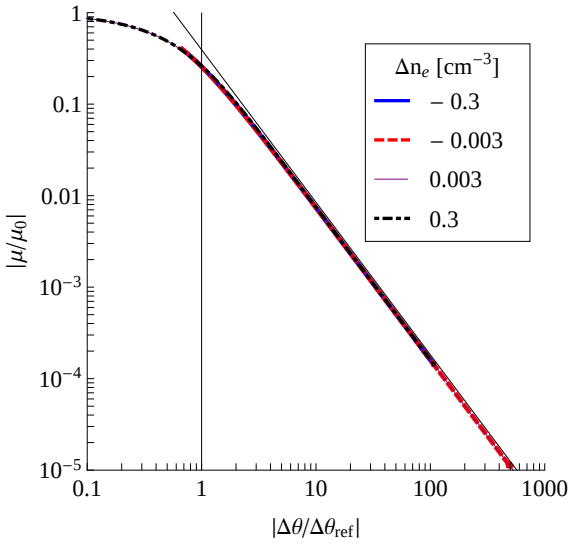

Figure 4. The ratio of the magnification of the fainter image, μ, to the magnification of the brighter image, μ_0, as a function of the angular separation, $\Delta\theta$, between two images formed at a single fold, scaled by the reference value, $\Delta\theta_{\rm ref}$. The legend indicates the difference between the electron density inside and outside the lens, Δn_e when the radius of curvature and thickness of the lens are assumed to be 4.1 kpc and 0.03 AU respectively. The reference separations are 0.75 and 4.73 mas for Δn_e of ± 0.003 and ± 0.3 cm^{-3} respectively, and the solid black line shows the analytical relation at large separations, equation (25). After these shifts in angular separation, the curves for various values of Δn_e lie directly on top of one another, although the curves for an overdense sheet extend to smaller angular separations due to the minimum angular separation in the convergent, underdense, case. This allows one to measure the parameter describing the lens, $\Delta n_e \theta_T \sqrt{\theta_R}$, up to the sign of Δn_e, from measurements of $|\mu/\mu_0|$ and $\Delta\theta$ by determining the reference separation required to align the point with the curves. Further observations, such as the change in angular separation with wavelength, can then be used to determine whether the lens is overdense or underdense. (See Section 3.1.) We also note a cutoff at large angular separations, which occurs earlier for $\Delta n_e = 0.3$ cm^{-3} that is due to a maximum angular separation determined by the thickness of the lens, as discussed in Section 3.2.

of its lensing screens (Liu et al. 2016), which gives an angular relative velocity of 1.16 mas/week. From the sign of the Doppler frequency of the point in the secondary spectrum created by the interference between these two images, we know whether the angular separation between the images is increasing or decreasing. If the Doppler frequency is negative, then the pulsar is moving away from the fainter, lensed image and the angular separation is increasing. If the Doppler frequency is positive, then the pulsar is moving towards the fainter, lensed image, and the angular separation is decreasing. Let's assume that the Doppler frequency is positive, and the angular separation is decreasing as the pulsar moves towards the apex of the fold and the magnification ratio increases. In the case of the convergent, underdense lens, after 4 weeks, the angular separation between the two images has decreased by 4.6 mas, and the magnification of the lensed image is 0.027. In the case of the divergent, overdense lens, after 4 weeks, the magnification ratio of the 2 images has increased to 0.029, and the angular separation has decreased by 4.7 mas. The magnification ratio of the images will continue to increase until a caustic forms after 7.4 weeks. After the caustic has formed, the lensed image (and the corresponding points in the secondary spectrum) will disappear. With VLBI measurements of the scattering screen, which have angular precisions on the order of 0.1 mas (Brisken et al. 2010), these changes are measurable.

Similarly, we can consider changes with frequency. Using the same example, we examine how the angular separation between the two images varies over a 32 MHz frequency band from 310.5 MHz to 342.5 MHz and find that, for the convergent lens, the angular separation will decrease by 0.019 mas moving from the lowest to highest frequencies in the band, while the magnification ratio decreases by 0.0012. For the divergent lens, the angular separation increases by 0.022 mas from the lowest to highest frequencies in the band, while $|\mu/\mu_0|$ decreases by 0.0013. We find that a power law is a very good fit to the relation between the angular separation and wavelength over this band, and we fit a power law for both the underdense and overdense lenses. The best fit power law exponents are shown in Table 1. A distinct difference between the overdense and underdense lenses arises here: In the underdense case, the power law exponent is positive, while in the overdense case it is negative. Brisken et al. (2010) measure positive power law exponents, 0.062 ± 0.006 and 0.019 ± 0.004, over this 32 MHz band for two of the three groups of arclets identified in the secondary spectrum of PSR B0834+06 (for the third group, they find that the separation is independent of wavelength within the measurement uncertainties), suggesting that these structures are underdense and indicating that the small exponents predicted by this model are measurable.

Table 1. Power law fits of the form $\Delta\theta = B\lambda^{\gamma}$ to the modelled change in separation with wavelength for a lens that produces two images with an angular separation of 10 mas and a flux ratio of 0.01 at 314.5 MHz. The fit is done over 310.5 MHz to 342.5 MHz. We have not included errors in our models, so the uncertainties on these parameters represent how well-approximated the intrinsic function is by a simple power law. While the exponents here are small, exponents of the same order of magnitude have been measured over the same bandwidth with 10 to 20% uncertainties by Brisken et al. (2010).

Δn_e [cm^{-3}]	γ
-0.0018	0.01910(3)
0.0018	-0.02239(4)

3.2 The Thickness of the Sheet

So far, we have only considered the regime $\theta > \theta_T/2$, where there are two distinct arms of the lens. However, we can glean additional information by considering the behaviour of the lens within $|\theta| < \theta_T/2$. The maximum extent of the lens along the line-of-sight occurs at $\theta = \theta_T/2$, so that the gradient $\nabla_x Z$ has opposite sign for $|\theta| < \theta_T/2$ and $\theta > \theta_T/2$, and therefore the bending angle, which is proportional to this gradient, switches direction at $\theta = \theta_T/2$. Because of this, the region $|\theta| < \theta_T/2$ acts as an additional lens with a different convergence than the portion of the fold discussed above. In principle, the pulsar can also be lensed by this region, creating additional images. However, these images are expected to be quite faint. While we do not expect the simplified constant density model of the fold that we have been using so far to hold in this regime, we can use it to provide a sense of the expected magnifications. We find that the images created in this regime are expected to have magnifications many orders of magnitude less than 1, and therefore we safely neglect images from this region.

Consider the case where we are observing two images and the faint image is from a region $\theta > \theta_T/2$ and moving towards smaller θ, while the angular separation of the two images is increasing. When the image reaches $\theta = \theta_T/2$, the lens will no longer bend the light into our line-of-sight, and the image will disappear. This sets a minimum angular position for the lensed image, $\theta_{\rm min} = \theta_T/2$, and a maximum angular separation between the two images. If the maximum angular separation could be observed, from the angular separation and the fluxes we could determine the parameter of the lens, the true position β, and the lensed position $\theta_{\rm min} = \theta_T/2$, as shown above. If we know the distance to the lens, we can also calculate the physical thickness of the lens, T. For the parameters chosen in Section 2.1, the maximum angular separation is 1250 mas for $\Delta n_e = \pm 0.03$ cm^{-3}, at which the flux ratio between the two images is $2\text{x}10^{-5}$, so the maximum angular separation is not expected to be observable.

4 CONCLUSIONS

In this paper, we have investigated the effects of a folded plasma sheet, such as a current sheet folded by Alfvén waves as proposed by Pen & Levin (2014) as a mechanism for pulsar scintillation. Using simple geometric optics, we calculate the number of images and magnifications of these images as a pulsar moves behind a fold in one of these sheets. We find that in the limit $\theta \ll \theta_R$ the lens can be described by a single parameter, $\Delta n_e\, \theta_T \sqrt{\theta_R}$, which can be constrained from observations of the pulsar. Once this parameter is known, this model can be used to predict how the fluxes and locations of the images will change over time and frequency, providing a concrete test of this model. In particular, we see that over a small band of 32 MHz we expect changes in the locations of the images measurable with VLBI and comparable to those measured by Brisken et al. (2010). We also see that we expect very different changes between an overdense sheet (divergent lens) and an underdense sheet (convergent lens): In the divergent lens, the angular separation between two images increases at higher frequencies, while in the convergent lens, it decreases at higher frequencies. Brisken et al. (2010) find that the separation decreases with frequency for two of three identified groups of images in the secondary spectrum of PSR B0834+06, suggesting an underdense, convergent lens. There are other qualitative differences between the convergent and divergent lens cases: caustics occur only when the fold is overdense and acts as a divergent lens, both images of the pulsar disappear when the pulsar is just behind the crest of the fold in the divergent case, and only the divergent lens produces inverted images. Dai & Venumadhav (2017) find that the waveforms of an inverted image are deformed. This distortion is expected to manifest in the scintillation pattern, so that it may be it possible to test if the observed images are inverted.

This model differs qualitatively from previous attempts to model ESEs and pulsar scintillation by varying electron column densities: If the sheet was infinitely thin, the electron column density profile we consider would diverge at the apex of the fold, so that our model does not adhere to the odd image theorem, and only two images are formed in some cases. Even though we include a finite thickness in our model, it is sufficiently small that the third image is too faint to be observed, and we effectively observe only two images, while other authors (*e.g.* Clegg et al. 1998; Pen & King 2012; Tuntsov et al. 2015; Bannister et al. 2016) have considered smoothly varying electron column densities, which adhere to the odd image theorem and produce one or three images. Although we have focused on pulsar scintillation, this model may also be applicable to ESEs. If two folds extend in opposite directions on the sheet and connect along the line-of-sight so that the folded sheet lies along the curve $x = z^3$, we expect a caustic at $x = 0$, and symmetric lensing behaviour about $x = 0$.

In practice, we observe a single pulsar lensed by many compact structures in the ISM, such as multiple folds along the current sheet. Each fold may have a different value of $\Delta n_e \theta_T \sqrt{\theta_R}$, and so the analysis above can be done for every fold, or equivalently every inverted arclet in the secondary spectrum. We can also look at phenomena that arise only when we have lensing from multiple folds, such as the the scattering tail of a pulse from the pulsar, the spread of pulse power over time due to the delays imparted by the various folds. However, this requires a more in depth analysis, including numerical simulations that take into account the distribution of waves along the sheet.

In future work, we will apply this test to observations of pulsar scintillation. The simplest test comes from observations of pulsars with well-defined inverted arclets in their

secondary spectra, as these arclets can be mapped to images on the sky through VLBI observations (Brisken et al. 2010) and therefore to individual folds in the current sheet. Ideal observations will be at low frequencies, where scintillation effects are strongest, and over a wide bandwidth, in order to measure the changes in the secondary spectrum over frequency with the best accuracy. As a second test, we can also consider changes in the secondary spectrum over time. For this, we desire many observations of the pulsar on week to month long timescales. Finally, we can simulate and test features of this model that arise when we consider many images of a single pulsar being created by multiple folds, such as the scattering tail of a highly scattered pulsar. The results of these tests will indicate the consistency of the folded current sheet model with observations of pulsar scintillation.

ACKNOWLEDGEMENTS

We thank Marten van Kerkwijk for many helpful comments on earlier drafts of this work. DS acknowledges funding from NSERC. The Dunlap Institute for Astronomy and Astrophysics is funded through an endowment established by the David Dunlap family and the University of Toronto.

References

Bannister K. W., Stevens J., Tuntsov A. V., Walker M. A., Johnston S., Reynolds C., Bignall H., 2016,] 10.1126/science.aac7673

Brisken W. F., Macquart J.-P., Gao J. J., Rickett B. J., Coles W. A., Deller A. T., Tingay S. J., West C. J., 2010, The Astrophysical Journal, 708, 232

Clegg A. W., Fey A. L., Lazio T. J. W., 1998, The Astrophysical Journal, 496, 253

Cordes J. M., Rickett B. J., Stinebring D. R., Coles W. A., 2006, The Astrophysical Journal, 637, 346

Dai L., Venumadhav T., 2017, arXiv:1702.04724 [astro-ph, physics:gr-qc]

Fiedler R. L., Dennison B., Johnston K. J., Hewish A., 1987, Nature, 326, 675

Hill A. S., Stinebring D. R., Barnor H. A., Berwick D. E., Webber A. B., 2003, The Astrophysical Journal, 599, 457

Hill A. S., Stinebring D. R., Asplund C. T., Berwick D. E., Everett W. B., Hinkel N. R., 2005, The Astrophysical Journal Letters, 619, L171

Liu S., Pen U.-L., Macquart J.-P., Brisken W., Deller A., 2016, Monthly Notices of the Royal Astronomical Society, 458, 1289

Pen U.-L., King L., 2012, Monthly Notices of the Royal Astronomical Society, 421, L132

Pen U.-L., Levin Y., 2014, Monthly Notices of the Royal Astronomical Society, 442, 3338

Putney M. L., Minter A. H., Stinebring D. R., Ransom S. M., 2005. p. 183.15, http://adsabs.harvard.edu/abs/2005AAS...20718315P

Stinebring D., 2007. p. 254, http://adsabs.harvard.edu/abs/2007ASPC..365..254S

Stinebring D. R., McLaughlin M. A., Cordes J. M., Becker K. M., Goodman J. E. E., Kramer M. A., Sheckard J. L., Smith C. T., 2001, The Astrophysical Journal Letters, 549, L97

Tuntsov A. V., Walker M. A., Koopmans L. V. E., Bannister K. W., Stevens J., Johnston S., Reynolds C., Bignall H. E., 2015, arXiv:1512.03411 [astro-ph]

Walker M., Melrose D., Stinebring D., Zhang C., 2004, Monthly Notices of the Royal Astronomical Society, 354, 43

This paper has been typeset from a TEX/LATEX file prepared by the author.